Hairpin vortices and highly elongated flow structures in a stably-stratified shear layer

Tomoaki Watanabe[1]†, James J. Riley[2], Koji Nagata[1], Keigo Matsuda[3] and Ryo Onishi[3]

[1]Department of Aerospace Engineering, Nagoya University, Nagoya 464-8603, Japan

[2]Department of Mechanical Engineering, University of Washington, Seattle, USA

[3]Center for Earth Information Science and Technology (CEIST), JAMSTEC, Yokohama 236-0001, Japan

(Received xx; revised xx; accepted xx)

Turbulent structures in stably-stratified shear layers are studied with direct numerical simulation. Flow visualization confirms the existence of hairpin vortices and highly elongated structures with positive and negative velocity fluctuations, whose streamwise lengths divided by the layer thickness are $\mathcal{O}(10^0)$ and $\mathcal{O}(10^1)$, respectively. The flow at the wavelength related to these structures makes a large contribution to turbulent kinetic energy. These structures become prominent in late time, but with small buoyancy Reynolds number indicating suppression of turbulent mixing. Active turbulent mixing associated with the hairpin vortices, however, does occur. The structures and the vertical profile of the integral shear parameter show connections between stable stratified shear layers and wall-bounded shear flows.

1. Introduction

Turbulent flows in the natural environment often evolve under the influences of ambient current shear and stable density stratification. For example, stably-stratified shear layers have been observed in the oceans and in the atmosphere (Woods 1968; De Silva *et al.* 1996), where the shear can produce turbulence that can promote large rates of mixing. These observations in field experiments have led many researchers to study stably-stratified shear layers with theories, laboratory experiments and numerical simulations, as summarized in review articles (Thorpe 1973*b*; Fernando 1991; Peltier & Caulfield 2003).

Laboratory experiments and numerical simulations often consider a stably-stratified shear layer where shear and stratification are localized in a thin layer, across which both mean velocity and density vary in the vertical direction (Thorpe 1973*a*; Smyth & Moum 2000*b*; Brucker & Sarkar 2007; Mashayek & Peltier 2012*a*,*b*). Many studies on stratified shear layers have been devoted to understanding instabilities and transition to turbulence. When the initial bulk Richardson number is lower than a critical value, turbulence is generated by the Kelvin-Helmholtz instability and causes mixing of the fluids of different densities (Strang & Fernando 2001). The development of the stably-stratified shear layer results in a density profile that is consistent with some observations in the oceans (Moum

† Email address for correspondence: watanabe.tomoaki@c.nagoya-u.jp

1996; Smyth & Moum 2000*b*). The generated turbulence ultimately begins to rapidly decay with time under the influence of stable stratification. Smyth & Moum (2000*b*) have also investigated the evolution of various length scales for a wide range of Reynolds number, Richardson number and Prandtl number. Mashayek *et al.* (2017) have shown the relation between the characteristics of turbulent mixing and various length scales and parameters of the stably-stratified shear layers for much larger Reynolds number than in Smyth & Moum (2000*b*).

Turbulence is often studied in terms of its coherent structures. These structures are typified by their length scales and characteristic coherent patterns, which are extended in space and time (Pope 2000). It is often sought to understand and explain a flow field in terms of a small number of these structures. Various structures have been identified in wall-bounded shear flows, such as low-speed streaks, outward ejections of low-speed fluid and hairpin-shaped vortical structures (Robinson 1991). These structures have been extensively studied by both numerical simulations and experiments (e.g., Head & Bandyopadhyay 1981; Zhou *et al.* 1999; Adrian *et al.* 2000; Schoppa & Hussain 2002; Carlier & Stanislas 2005; Wu & Moin 2009). Previous studies have also found highly elongated flow structures, with both positive and negative streamwise velocity fluctuations, which are termed "superstructures" in turbulent boundary layers (Hutchins & Marusic 2007) and "very large-scale motions" in turbulent pipe flows (Kim & Adrian 1999). These long flow structures are shown to be important, with significant turbulent kinetic energy (Hutchins & Marusic 2007), and their influence on small-scale features near a wall is noteworthy, as reported by Mathis *et al.* (2009). More studies on these very long structures in wall turbulence can be found, for example, in Monty *et al.* (2007, 2009); Hellström *et al.* (2011); Wu *et al.* (2012); Lee & Sung (2013).

The present study investigates the flow structures in a stably-stratified shear layer with localized shear and stratification. Direct numerical simulations (DNS) in a very large computational domain allow us to explore large-scale structures as well as smaller-scale ones in a turbulent stably-stratified shear layer. Our DNS confirms the existence of hairpin-shaped vortices and highly elongated structures with positive and negative streamwise velocity fluctuations, both of which are similar to the structures found in wall-bounded shear flows. The flow associated with the hairpin vortices is shown to contribute the vertical transfer of momentum and density even when the Kolmogorov scale is of the same order of the Ozmidov scale.

In the next section we discuss the details of our simulation methodology, and some of the important dimensional and non-dimensional parameters in the problem. In the subsequent section we then present in detail our results, and in the final section we summarize our conclusions from this study.

2. Direct numerical simulations of stably-stratified shear layer

We consider temporally-evolving, stably-stratified shear layers with localized shear and stratification (Smyth & Moum 2000*b*), which have also been studied with different parameters by DNS in our previous papers; details of our results and methodology can be found in Watanabe *et al.* (2016, 2017). The streamwise, spanwise and vertical directions are represented by x, y and z, respectively, and the corresponding components of the velocity vector are u, v and w. The density field is expressed as $\rho_a + \rho(x, y, z; t)$, with ρ_a a constant reference value, and the deviation from ρ_a denoted by ρ. The governing equations are the Navier–Stokes equations with the Boussinesq approximation, written

as

$$\frac{\partial u_j}{\partial x_j} = 0, \tag{2.1}$$

$$\frac{\partial u_i}{\partial t} + \frac{\partial u_i u_j}{\partial x_j} = -\frac{1}{\rho_a}\frac{\partial p}{\partial x_i} + \nu\frac{\partial^2 u_i}{\partial x_j \partial x_j} - g\frac{\rho}{\rho_a}\delta_{i3}, \tag{2.2}$$

$$\frac{\partial \rho}{\partial t} + \frac{\partial u_j \rho}{\partial x_j} = \kappa\frac{\partial^2 \rho}{\partial x_j \partial x_j}, \tag{2.3}$$

where the integers $i, j = 1$, 2 and 3 denote the x, y and z directions, ν is the kinematic viscosity, κ is the diffusivity coefficient for density, and g is the gravitational acceleration. The gravitational force appears in the momentum equation in the z direction.

The flow develops with time in a computational domain that is taken to be periodic in both horizontal directions. The initial mean streamwise velocity is given by $\langle u \rangle = 0.5U_0 \tanh(2z/h_0)$, where $\langle \cdot \rangle$ is an averaged value taken on a homogeneous plane, U_0 is the velocity difference across the shear layer and h_0 is the initial shear layer thickness. The initial mean velocity is zero for v and w. The initial velocity field is obtained by superimposing velocity fluctuations onto the mean velocity as $u = \langle u \rangle + u'$, $v = v'$ and $w = w'$, where fluctuations u', v' and w' are obtained by a diffusion process that converts random noise to spatially correlated fluctuations (Kempf *et al.* 2005). The initial density field is given as $\rho = -0.5\rho_0 \tanh(2z/h_0)$ without any density perturbation, where ρ_0 is the density difference across the stably-stratified shear layer.

The flow is characterized by three non-dimensional parameters: the Reynolds number $Re = U_0 h_0/\nu$, the Prandtl number $Pr = \nu/\kappa$ and the bulk Richardson number $Ri = g\rho_0 h_0/\rho_a U_0^2$. Pr affects the ratio between the smallest length scales of velocity and density fields, where this ratio is expected to be $\mathcal{O}(1)$ in the case of $Pr = 1$. For simplicity, all the simulations are conducted with $Pr = 1$ for investigating dependence of the flow on Re and Ri. Because the smallest length scale of density fluctuations decreases as Pr increases, larger Pr requires smaller grid spacing in the DNS, which increases the computational cost. The DNS are conducted in a computational domain with the size of $(L_x \times L_y \times L_z) = (448h_0, 84h_0, 140h_0)$, which is discretized by $(N_x \times N_y \times N_z)$ grid points. This computational domain is much larger than the roller vortices arising from the Kelvin-Helmholtz instability. Previous numerical simulations of stratified shear layers sometimes used a computational domain whose streamwise extent is comparable to the roller vortices, because these studies mainly investigated the instabilities and transition (Smyth & Moum 2000*b*; Mashayek & Peltier 2012*a*). A significantly larger domain than most in previous numerical simulations is used in this study since its purpose is to investigate large-scale structures that appear after the transition. Uniform grid spacing is used in both horizontal directions, while the grid is stretched in the vertical direction near the vertical boundaries using a mapping function employed by Watanabe *et al.* (2018), while a finer grid is employed near the shear layer. The grid size near the centreline is set to be the same for all three directions, i.e. $\Delta_x = \Delta_y = \Delta_z$. Periodic boundary conditions are applied in the two horizontal directions, while the free-slip boundary conditions are applied to the velocity, and zero-flux conditions to the density, at the top and bottom of the computational domain.

The DNS code is the same as the one used for stratified shear layers in Watanabe *et al.* (2016, 2017, 2018). The code is based on the fractional step method. Second and fourth order fully-conservative central difference schemes are used in the vertical and horizontal directions, respectively, while a third-order Runge-Kutta method is used for

Table 1: Parameters for the DNS of stably-stratified shear layers. The table also presents values for δ_u, L_O, η, Re_b, Ri_g and L_ε at $z = 0$ and $t = 320t_r$.

	Re20Ri6	Re12Ri8	Re12Ri6	Re12Ri3
Re, Ri	$2000, 0.06$	$1200, 0.08$	$1200, 0.06$	$1200, 0.03$
N_x, N_y, N_z	$12288, 2304, 1200$	$7776, 1458, 850$	$7776, 1458, 850$	$7776, 1458, 850$
$[\Delta_x/\eta]_{max}$	1.9	2.0	2.0	1.9
δ_u	$10.3h_0$	$9.0h_0$	$10.6h_0$	$14.5h_0$
L_O	$0.12h_0$	$0.05h_0$	$0.11h_0$	$0.69h_0$
η	$0.056h_0$	$0.10h_0$	$0.085h_0$	$0.054h_0$
Re_b	2.7	0.4	1.4	28.6
Ri_g	0.47	0.52	0.49	0.35
L_ε	$8.3h_0$	$12.6h_0$	$9.3h_0$	$10.7h_0$

temporal advancement. The Poisson equation for pressure is solved using the Bi-CGSTAB method.

Four simulations are carried out with parameters summarized in table 1. Most of the results presented are for case Re20Ri6, while other simulations are used for examining the effects of Re and Ri. Averages taken on a horizontal plane $\langle\cdot\rangle$ are obtained as functions of the vertical location and time. In this paper, a fluctuation of variable f from the average $\langle f\rangle$ is denoted as $f' = f - \langle f\rangle$.

Important length scales and non-dimensional numbers used in the discussion are defined here. The mean velocity $\langle u\rangle$ increases in the z direction from $-0.5U_0$ to $0.5U_0$ across the shear layer. Therefore, the shear layer thickness δ_u can be estimated as the distance between vertical locations of $\langle u\rangle = 0.49U_0$ and $\langle u\rangle = -0.49U_0$. An integral length scale of the flow is defined as

$$L_\varepsilon = q^3/\varepsilon, \tag{2.4}$$

where $q^2 = \langle u_i' u_i'\rangle$ is twice of the turbulent kinetic energy, $\varepsilon = 2\nu\langle s_{ij}' s_{ij}'\rangle$ is the turbulent kinetic energy dissipation rate and s_{ij}' is the fluctuating rate-of-strain tensor. The mean vertical shear and the buoyancy frequency are defined as $S = \langle\partial u/\partial z\rangle$ and $N = \sqrt{-(g/\rho_a)\langle\partial\rho/\partial z\rangle}$, respectively. One of the important length scales in stably-stratified turbulence is the Ozmidov scale, defined by

$$L_O = \sqrt{\varepsilon/N^3}. \tag{2.5}$$

The Ozmidov scale is considered to be the smallest length scale that is affected by buoyancy, so that vertical motions at scales greater than the Ozmidov scale are strongly suppressed under stable stratification. On the other hand, the smallest length scale of turbulence is the Kolmogorov scale, defined by

$$\eta = (\nu^3/\varepsilon)^{1/4}. \tag{2.6}$$

In the present DNS, the Kolmogorov scale takes its smallest value at $t \approx 100t_r$ ($t_r = h_0/U_0$), and then increases with time because of the decay of ε (Smyth & Moum 2000*b*). The table shows the maximum values of Δ_x/η on the centreline during the simulation. All simulations are performed with $\Delta_x/\eta \leqslant 2.0$, which is small enough for the central difference schemes used in the DNS to adequately capture the dissipation spectrum of these turbulent flows (Watanabe *et al.* 2018). The table also shows δ_u and centreline

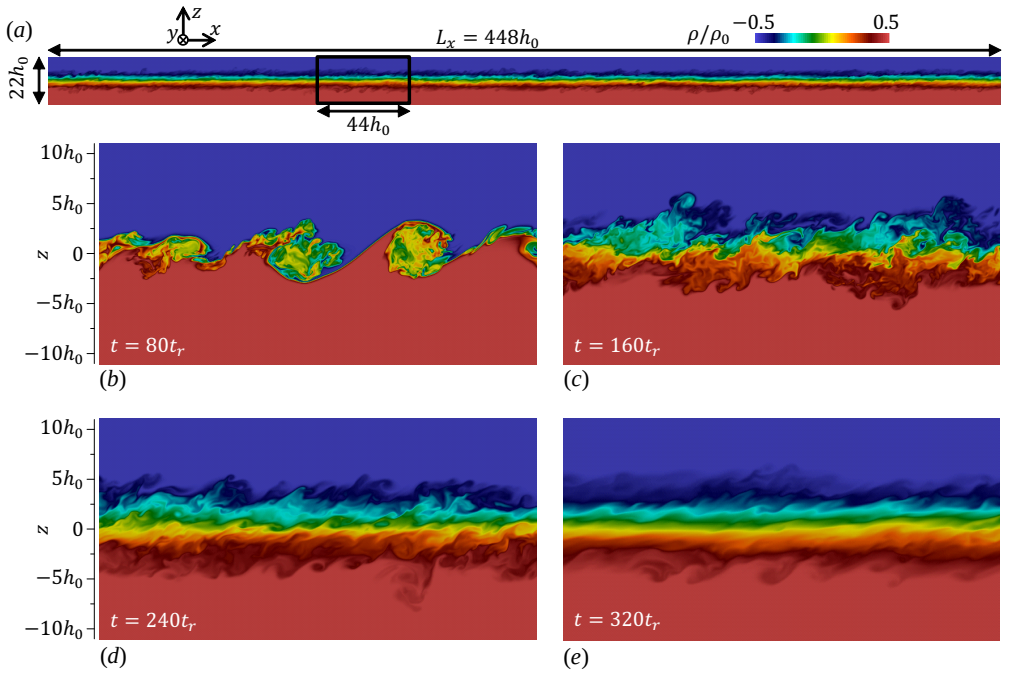

Figure 1: From the DNS of a temporally-evolving, stably-stratified shear layer (Re20Ri6). (*a*) Density field at $t = 320t_r$ in an x-z plane which includes the full length of the computational domain in the streamwise direction. Density field in the region marked by the box in (*a*) at (*b*) $t = 80t_r$, (*c*) $160t_r$, (*d*) $240t_r$ and (*e*) $320t_r$. The total extent of the computational domain in the vertical (z) direction is not shown.

values of L_ε, L_O and η at $t = 320t_r$. δ_u decreases as Ri increases, although it only weakly depends on Re for Ri and Re considered in this study. The gradient Richardson number Ri_g and buoyancy Reynolds number Re_b are defined as

$$Ri_g = N^2/S^2, \tag{2.7}$$

$$Re_b = (L_O/\eta)^{4/3} = \varepsilon/\nu N^2. \tag{2.8}$$

As can be seen in its definition, Re_b takes a large value when the Ozmidov scale is much greater than the Kolmogorov scale. In this case, there is a range of turbulent length scales for which direct influences of buoyancy are not significant. On the other hand, $Re_b = \mathcal{O}(10^0)$ results in suppression of turbulent motions at all scales because then $L_O \sim \eta$, for which motions at the smallest turbulent length scale are also strongly influenced by buoyancy. Re_b is also used as a measure of intensity of turbulence in oceanography (Barry *et al.* 2001; Shih *et al.* 2005; de Lavergne *et al.* 2016). The table also shows the gradient Richardson number Ri_g and buoyancy Reynolds number Re_b at $t = 320t_r$ on the centreline. The temporal evolutions of δ_u, L_O, η, Ri_g and Re_b are shown in the next section.

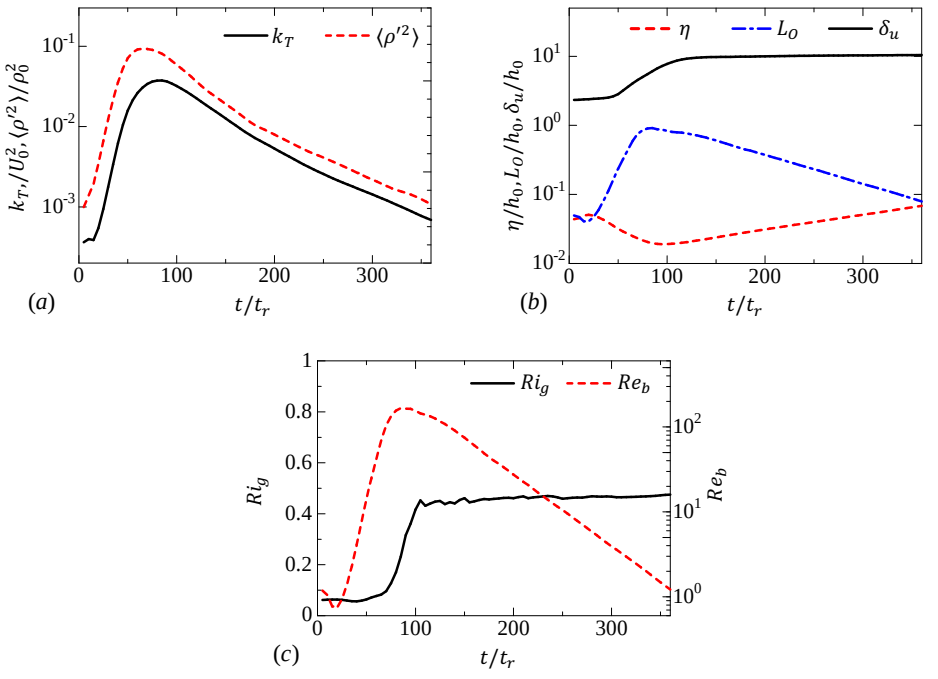

Figure 2: The evolution of statistics in a temporally-evolving, stably-stratified shear layer (Re20Ri6). (a) turbulent kinetic energy k_T and density fluctuation variance $\langle\rho'^2\rangle$, (b) Kolmogorov scale η, Ozmidov scale L_O and shear layer thickness δ_u, and (c) buoyancy Reynolds number Re_b and gradient Richardson number Ri_g.

3. Results and discussions

3.1. *Temporal evolution of stably-stratified shear layer*

Figure 1(a) visualises the density field ρ on an x-z plane at $t/t_r = 320$ for case Re20Ri6, while figures 1(b-e) show ρ at $t/t_r = 80$, 160, 240 and 320 in the box region shown in figure 1(a). It is seen that turbulence in the shear layer develops, due to Kelvin-Helmholtz instability, by $t/t_r = 80$. The roller vortices of the instability have already paired before $t/t_r = 80$. The streamwise length of the initial roller vortices before pairing, estimated from the density profile on an x-z plane, is about $2h_0$-$4h_0$ at $t/t_r = 40$ in all the DNS. The density field in figure 1(c) exbibits patterns associated with small scales of turbulence while density is more stratified in the shear layer at later time in figure 1(e).

Figure 2 shows temporal evolutions of statistics in case Re20Ri6. Figure 2(a) plots density fluctuation variance $\langle\rho'^2\rangle$ and turbulent kinetic energy $k_T = \langle u_i' u_i'/2\rangle$ on the centreline, while figure 2(b) plots the shear layer thickness δ_u, Kolmogorov scale η and Ozmidov scale L_O on the centreline. As the turbulent shear layer grows from $t = 0$, $\langle\rho'^2\rangle$, k_T and δ_u initially increase with time. Then the shear layer ceases the growth, as attested by the behaviour of δ_u for $t/t_r \geqslant 100$, and the density and velocity fluctuations then decay rapidly with time. As these fluctuations decay, the Kolmogorov scale and Ozmidov scale increase and decrease, respectively, as also reported in previous DNS studies (Smyth & Moum 2000b).

Figure 2(c) shows temporal evolutions of Ri_g and Re_b on the centreline for case Re20Ri6. Once the turbulent shear layer has developed, Ri_g becomes almost independent

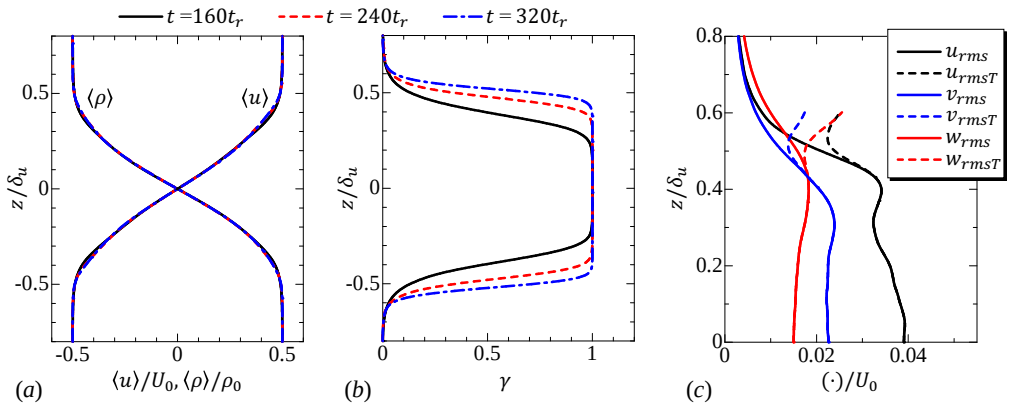

Figure 3: The vertical profiles of (a) mean streamwise velocity $\langle u\rangle$ and density $\langle\rho\rangle$, (b) intermittency factor and (c) rms velocity fluctuations defined with average over the turbulent fluid $\langle\cdot\rangle_T$ or with conventional average for case Re20Ri6. (c) shows the results at $t = 320t_r$.

of time, with the value of about 0.45. On the other hand, Re_b ultimately decreases with time from $\mathcal{O}(10^2)$ to $\mathcal{O}(10^0)$, implying that turbulent motions at very small scales also become directly affected by buoyancy, as the Ozmidov scale becomes as small as the Kolmogorov scale. Salehipour *et al.* (2015) showed that the decay of Re_b in late time is hardly affected by the Prandtl number for $1 \leqslant Pr \leqslant 16$ in the stably stratified shear layers. Further details of stratified shear layer development can be found in previous studies (Smyth & Moum 2000*b*; Brucker & Sarkar 2007; Watanabe *et al.* 2016, 2017; Mashayek *et al.* 2017).

Figure 3(a) shows the vertical profiles of $\langle u\rangle$ and $\langle\rho\rangle$, where the vertical coordinate is normalized by the shear layer thickness δ_u. The normalized profiles of $\langle u\rangle$ and $\langle\rho\rangle$ hardly change with time from $t = 160t_r$ to $320t_r$. Turbulent shear layers are known to be intermittent, and a flow can be turbulent or non-turbulent at a fixed location. Since turbulent structures are investigated in this study, it is important to show the spatial distribution of turbulent fluids in the stably-stratified shear layer. Because a turbulent flow is characterized by its vorticity (Corrsin & Kistler 1955), the turbulent region in the stably-stratified shear layer can be detected as the region with $|\boldsymbol{\omega}| \geqslant \omega_{th}$, where $|\boldsymbol{\omega}|$ is magnitude of vorticity vector and ω_{th} is a suitably chosen threshold value (Watanabe *et al.* 2016). The turbulent region also has higher kinetic energy dissipation rate than the non-turbulent region. The difference between turbulent and non-turbulent regions is clearer for vorticity magnitude (enstrophy) than kinetic energy dissipation rate in free shear flows (da Silva & Pereira 2008). This is why the vorticity magnitude has been used for detecting the turbulent region in intermittent turbulent flows (da Silva *et al.* 2014). It should be noted that the regions outside of the shear layer have constant density values that do not support the propagation of internal gravity waves, unlike in turbulent shear layers developing in a stably-stratified fluid (Watanabe *et al.* 2018). The threshold value ω_{th} is determined based on the mean vorticity magnitude on the centreline, $\langle|\boldsymbol{\omega}|\rangle_C$, as $\omega_{th} = 0.04\langle|\boldsymbol{\omega}|\rangle_C$ following our previous studies on turbulent/non-turbulent interfaces in stably-stratified shear layers (Watanabe *et al.* 2016, 2017). An intermittency function $I(x, y, z)$ is defined to be $I = 1$ for a turbulent fluid and $I = 0$ for a non-turbulent fluid (Pope 2000). The intermittency factor γ, defined as the probability that the flow is turbulent, can be obtained by taking average of I as $\gamma = \langle I\rangle$. Figure 3$(b)$ shows the

vertical profile of γ at $t = 160t_r$, $240t_r$ and $320t_r$ for case Re20Ri6. The region near the centreline $z = 0$ has $\gamma = 1$, and the middle of the shear layer is always turbulent. At $t = 160t_r$, γ begins to decrease with $|z/\delta_u|$ for $|z/\delta_u| > 0.2$, as non-turbulent fluids appear in this region. At $t = 240t_r$ and $320t_r$, $\gamma < 1$ can be found for $|z/\delta_u| > 0.4$, and γ decreases with $|z/\delta_u|$ more sharply than at $t = 160t_r$. This confirms that the region where both turbulent and non-turbulent fluids coexist becomes narrower with time. This tendency is consistent with other observations that the turbulent/non-turbulent interface is flattened by the influence of stable stratification (Krug *et al.* 2015; Watanabe *et al.* 2016, 2017). From its definition, $\gamma = 0$ implies that there are no turbulent motions at a certain height. Therefore, figure 3(b) also indicates that turbulent motions reach up to $|z/\delta_u| \approx$ 0.6-0.7. At $t = 320t_r$, γ is about 0.05 at $|z/\delta_u| \approx 0.6$, and the region of $|z/\delta_u| > 0.6$ consists mostly of non-turbulent motions. Therefore, statistics related to turbulent structures are presented in the region of $|z/\delta_u| \leqslant 0.6$ in this paper.

The intermittency function I can be used for defining averages taken for turbulent fluids as $\langle f \rangle_T = \langle fI \rangle / \langle I \rangle$ (Pope 2000). Figure 3(c) shows the rms velocity fluctuations of the turbulent fluids, $u_{rmsT} = \sqrt{\langle u^2 \rangle_T - \langle u \rangle_T^2}$, $v_{rmsT} = \sqrt{\langle v^2 \rangle_T - \langle v \rangle_T^2}$ and $w_{rmsT} = \sqrt{\langle w^2 \rangle_T - \langle w \rangle_T^2}$, in the upper side of the shear layer ($z \geqslant 0$) at $t = 320t_r$. Here, the average for turbulent fluids is computed in the region with $\gamma \geqslant 0.05$. For comparison, the figure also shows the rms velocity fluctuations defined with the conventional average, $u_{rms} = \sqrt{\langle u^2 \rangle - \langle u \rangle^2}$, $v_{rms} = \sqrt{\langle v^2 \rangle - \langle v \rangle^2}$ and $w_{rms} = \sqrt{\langle w^2 \rangle - \langle w \rangle^2}$, which include the contribution from non-turbulent fluids. The difference between these two averaging procedures appears in the intermittent region with $0 < \gamma < 1$. In the middle of the shear layer ($|z/\delta_u| \leqslant 0.4$), the vertical velocity w has the smallest rms fluctuation, as expected from the suppression of vertical motions by stable stratification. In the region of $|z/\delta_u| \geqslant 0.4$, u_{rms}, v_{rms} and w_{rms} decrease in the vertical direction as the laminar flow exists outside the shear layer. The rms velocity fluctuations of turbulent fluids do not decrease in this region, and u_{rmsT}, v_{rmsT} and w_{rmsT} for $|z/\delta_u| \geqslant 0.4$ are comparable to the values near the centreline. It can be also seen that the vertical rms velocity fluctuation w_{rmsT} is as large as the horizontal ones (u_{rmsT} and v_{rmsT}), and vertical turbulent motions are more active near the edge of the shear layer than near the centreline.

3.2. *Flow structures in stably-stratified shear layers*

Figures 4(a-c) show the streamwise velocity fluctuations u' in the horizontal plane at the centre of the shear layer ($z = 0$) at different times. The characteristic length scales (e.g. Λ_L defined as the peak wavelength in energy spectra of streamwise velocity fluctuations in figure 11) of u' grow with time along with the increase in other characteristic length scales of turbulence, such as Kolmogorov scale defined in (2.6). It is also seen that the regions with positive or negative u' are highly elongated in the streamwise direction at later times. At $t = 320t_r$, the shear layer thickness is $\delta_u = 10.3h_0$, although the regions with positive or negative u' are extended to streamwise lengths of $\mathcal{O}(10^2 h_0)$. Figure 5 shows the density fluctuation ρ' on the centre plane ($z = 0$) at $t = 320t_r$. The regions with positive or negative ρ' are also elongated in the streamwise direction. Comparison between figures 4(c) and 5 shows that u' tends to be negatively correlated with ρ'. This can be explained by the profiles of mean velocity and density.

Small-scale vortical structures are investigated using the second invariant of the velocity gradient tensor, $Q = (\omega_i \omega_i - 2S_{ij}S_{ij})/4$, where ω_i is the vorticity vector and S_{ij} is the rate-of-strain tensor. Regions with $Q > 0$ are dominated by vortical motions rather than straining motions (Ooi *et al.* 1999; Davidson 2004). Figure 6(a) shows isosurfaces of a positive value of Q (white) along with isosurfaces of positive (red) and negative (blue)

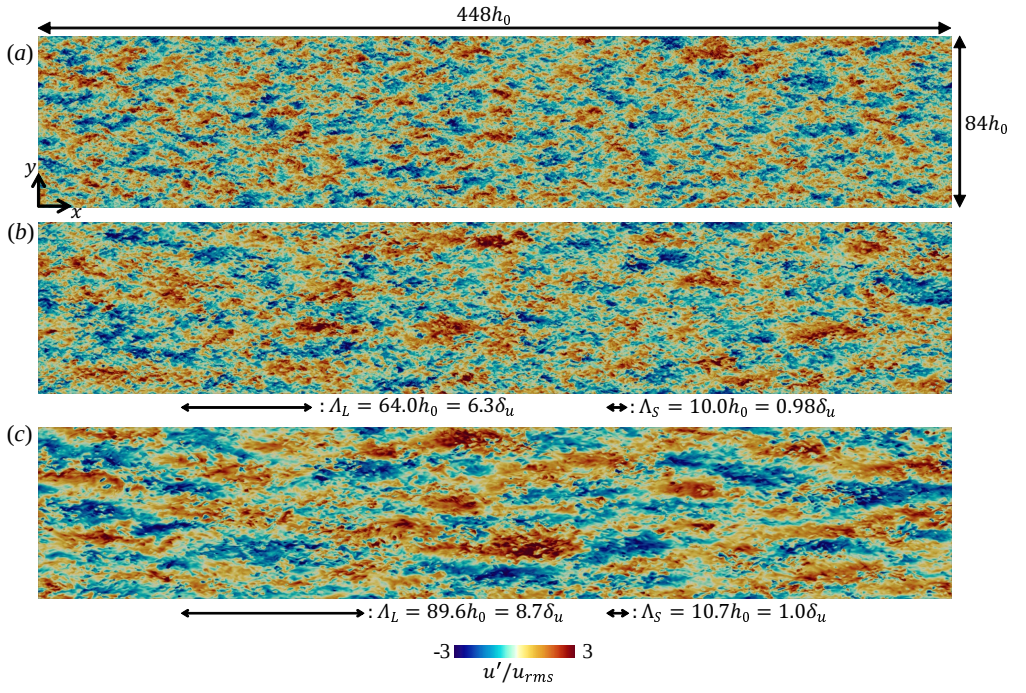

Figure 4: Streamwise velocity fluctuations on the x-y plane at the centre of the computational domain ($z = 0$) at (a) $t = 160t_r$, (b) $t = 240t_r$ and (c) $t = 320t_r$ for case Re20Ri6. Arrows under (b) and (c) represent wavelengths Λ_S and Λ_L at which the spectra of the streamwise velocity fluctuations $k_x E_{uu}$ have peaks (see figure 11).

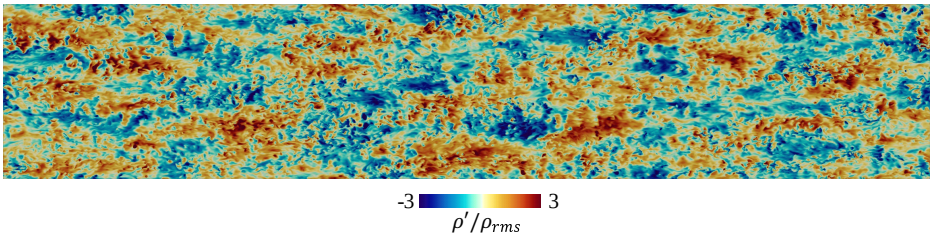

Figure 5: Density fluctuations on the x-y plane at the centre of the computational domain ($z = 0$) at $t = 320t_r$ for case Re20Ri6.

values of u' at the top of the shear layer. Note that the outer edge of the turbulent region appears in the region with $0 < \gamma < 1$ shown in figure 3(b). One can observe tube-like vortical structures given by the isosurfaces of Q in figure 6(a). One of the typical vortical structures in figure 6(a) is blown up and visualized in figure 6(b). This vortical structure has a shape similar to hairpin vortices found in wall turbulence (Adrian *et al.* 2000; Wu & Moin 2009). Most of the vortical structures in figure 6(a) have the shape of a hairpin vortex. A large number of hairpin vortices were also found in turbulent boundary layers at the momentum thickness Reynolds number $Re_\theta \approx 900$ (Wu & Moin 2009). The diameter of the vortex in figure 6(b) is several times of the Kolmogorov scale η, which is consistent with small-scale vortical structures of non-stratified turbulence (da Silva *et al.* 2011). Figure 6(c) shows colour contours of u' and the velocity fluctuation vector (u', w') on the x-z plane that crosses the head of the hairpin vortex. The region with low

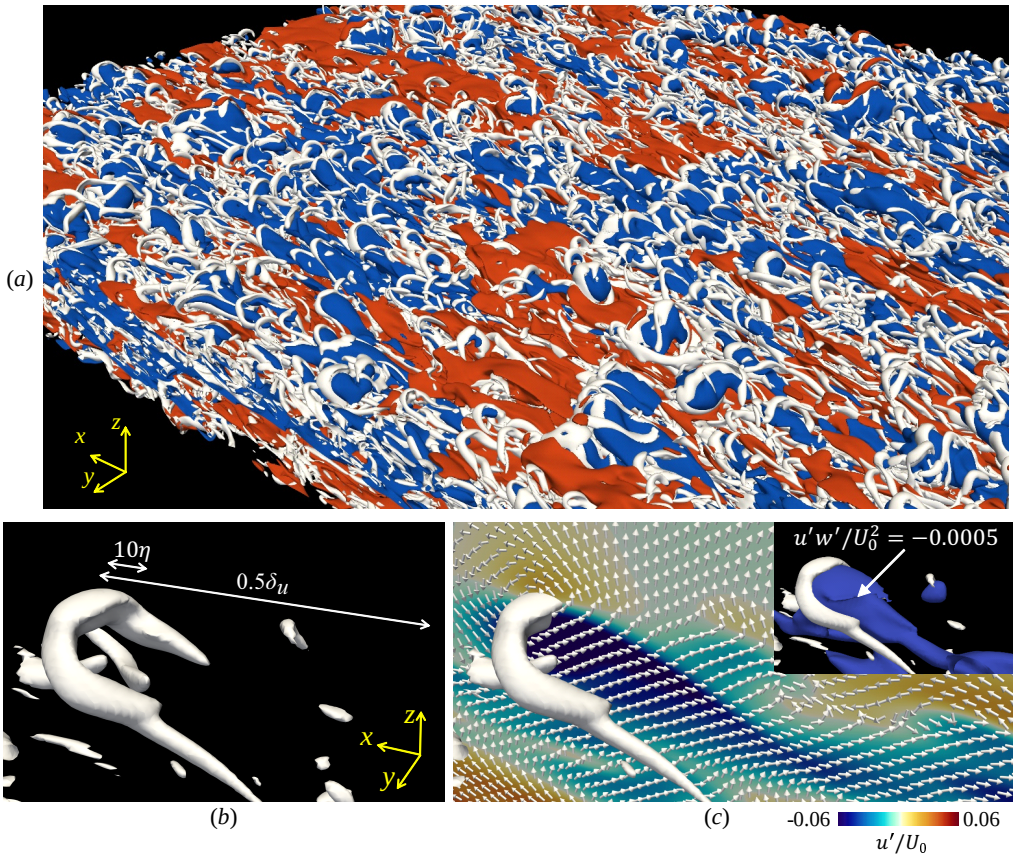

Figure 6: (a) Small-scale vortical structures (white), high-speed (red) regions, and low-speed (blue) regions visualized by isosurface of $Q/\langle S_{ij}S_{ij}\rangle_C = 0.2$, $u'/U_0 = 0.039$, and $u'/U_0 = -0.039$, respectively. $\langle S_{ij}S_{ij}\rangle_C$ is the averaged strain product on the centreline. (b) A hairpin vortex that appears at the top of the stably-stratified shear layer. (c) The same hairpin vortex is shown with colour contours of the streamwise velocity fluctuation u' and fluctuating velocity vector (u', w') on the x-z plane crossing the head of the hairpin vortex, where the top right also shows the isosurface of $u'w' = -0.0005U_0^2$. These results are taken from Re20Ri6 at $t = 320t_r$.

streamwise velocity $u' < 0$ appears between the legs of the hairpin vortex, and is extended in the streamwise direction over a length greater than $0.5\delta_u$. The vectors also indicate that the head of the hairpin vortex induces a rotating motion, which is also consistent with a velocity vector around the head of the hairpin vortex in wall turbulence (Adrian *et al.* 2000). Top right of figure 6(c) shows the isosurface of negative value of $u'w'$, which can be related to vertical momentum transfer and turbulent kinetic energy production. The region of $u'w' < 0$ appears below the head of the hairpin and between the legs, as expected for the hairpin vortex (Davidson 2004), and has a streamwise length scale that is comparable to the streamwise length of the hairpin vortex structure ($\sim \delta_u$). This streamwise length scale of vertical momentum transfer $u'w' < 0$ is much larger than the Ozmidov scale L_O, as can be found from the relation $\delta_u \gg L_O$ at $t = 320t_r$ in figure 2(b). At $t = 320t_r$, the buoyancy Reynolds number Re_b is 2.7 on the centreline. It is indicated

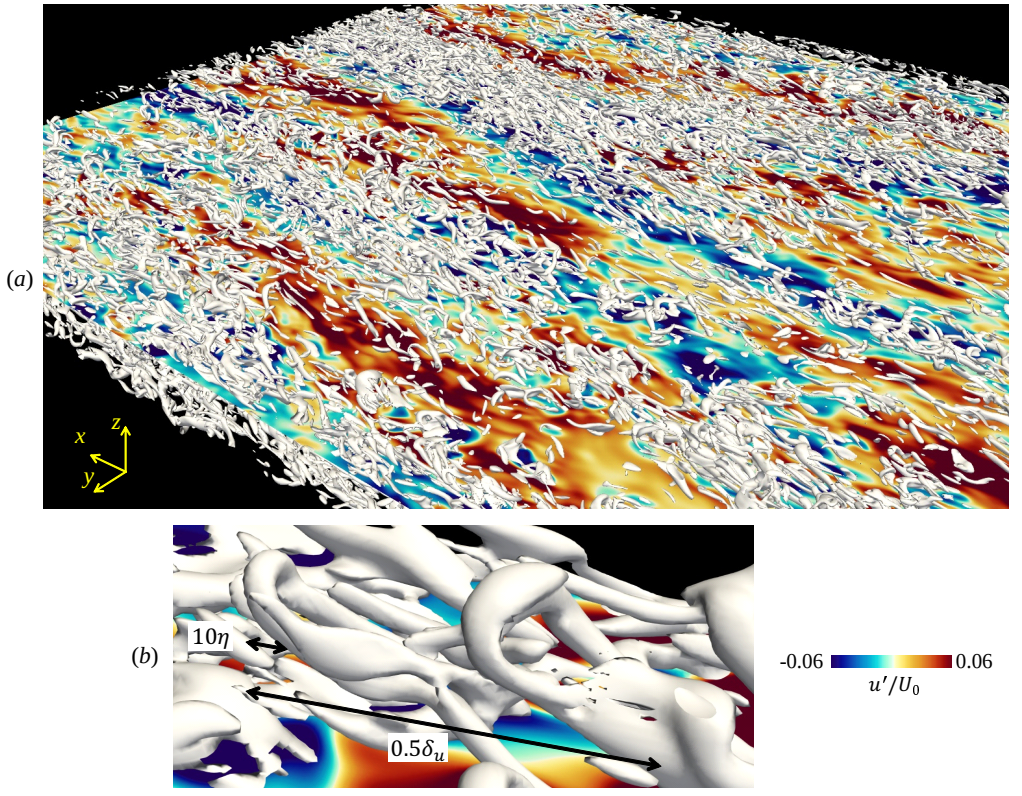

Figure 7: (a) Colour contours of the streamwise velocity fluctuation u' on the x-y plane at $z/h_0 = 0.5$ ($z/\delta_u = 0.05$) and small-scale vortical structures (isosurface of $Q/\langle S_{ij}S_{ij}\rangle_C = 0.2$) in the region of $z/h_0 \leqslant 2.3$ ($z/\delta_u = 0.22$). (b) Close-up of small-scale vortical structures in the middle of the stably-stratified shear layer in (a). These results are taken from Re20Ri6 at $t = 320t_r$.

that the hairpin vortex can cause vertical momentum transfer at large scales even for such a small value of Re_b.

Figure 7(a) shows isosurfaces (white) of a positive value of Q in the middle of the shear layer ($z \leqslant 0.22\delta_u$) along with colour contours of u' in the horizontal plane at $z = 0.02\delta_u$. Tube-like vortical structures can be found even in the middle of the shear layer for the isosurfaces of Q. Figure 7(b) shows a close-up of the vortical structures in the middle of the layer. One can also find hairpin vortices near the centreline. Their diameters are $\sim 10\eta$ and streamwise lengths $\sim \delta_u$, and the vortices are similar in the top and middle of the layer. The middle of the shear layer, shown in figure 7(b), has more vortices oriented in the streamwise direction than in the top of the shear layer, while the top of the shear layer has many heads (spanwise vortices) of the hairpin vortex, as seen in figure 6(a). Comparison between figures 6 and 7 shows that hairpin vortices are more prominent near the top of the shear layer than in the middle.

In figures 6(a) and 7(a), the distribution of the small-scale vortical structures with $Q > 0$ is intermittent. Specifically, in figure 6(a), small-scale vortical structures appear over the region with negative u' (blue). Both turbulent and non-turbulent fluids coexist at the top of the shear layer. The fluid with $u' < 0$ below the hairpin vortices in figure 6(a) is turbulent and has lower streamwise velocity than the non-turbulent fluid. On the

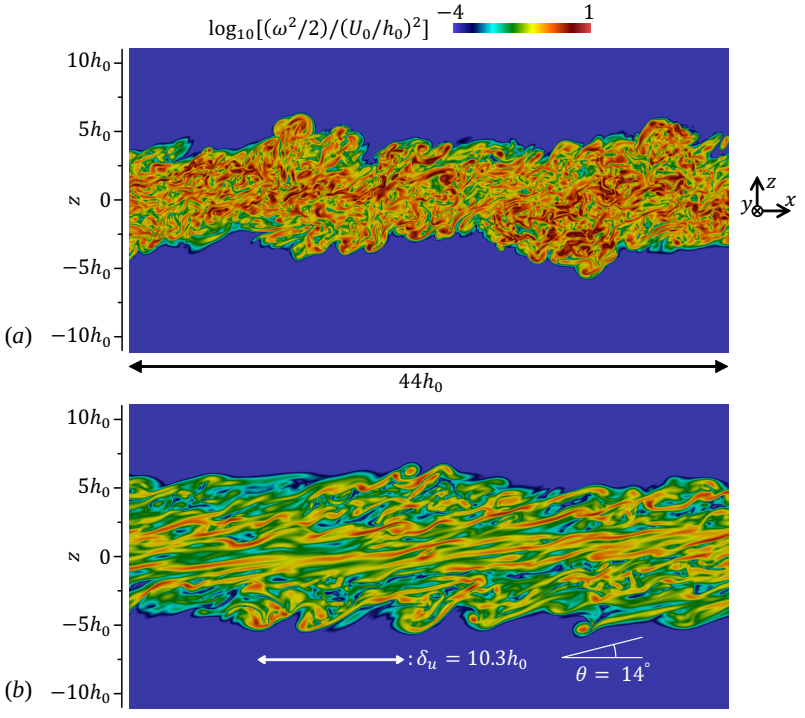

Figure 8: Enstrophy in an x-z plane at (a) $t = 160t_r$ and (b) $t = 320t_r$ for case Re20Ri6.

other hand, the high speed fluid in figure 6(a) is non-turbulent with negligible enstrophy $Q \approx -S_{ij}S_{ij}/2 \leqslant 0$. Therefore, small-scale vortices appear in the turbulent region with negative u'. Even in the middle of the shear layer in figure 7(a), less small-scale vortical structures appear above the region with $u' > 0$ (red). This is similar to the small-scale vortices that appear along with low-speed fluid in turbulent boundary layers (Dennis & Nickels 2011).

Figure 8 shows the enstrophy $\omega_i\omega_i/2$ in an x-z plane at $t = 160t_r$ and $320t_r$. The region with large enstrophy does not align in a specific direction at $t = 160t_r$, and the vortical structures with large enstrophy are oriented in various directions. On the other hand, the colour contours of $\omega_i\omega_i/2$ at $t = 320t_r$ show patterns of streamwise vortices in the middle of the shear layer and of the heads and legs of hairpin vortices near the edge of the shear layers. In figure 8(b), the streamwise vortices and the legs of hairpin vortices appear as thin and long regions of large $\omega_i\omega_i/2$ with the streamwise length of $\sim \delta_u$, while the heads of hairpin vortices can be identified as circular regions of large $\omega_i\omega_i/2$. One of the large enstrophy regions associated with a hairpin vortex makes an angle of 14 degrees with the streamwise direction as shown in figure 8(b). Thus, the hairpin vortex in this stably-stratified layer makes a lower angle than analogous vortices in wall turbulence, where the hairpin vortex is often oriented at 45 degrees from the mean flow direction (Head & Bandyopadhyay 1981). Reduction of the angle of hairpin vortices due to stable stratification was also reported in experiments of stably-stratified boundary layers (Williams 2014).

In figures 6 and 7, the vortices are detected as the regions with $Q/\langle S_{ij}S_{ij}\rangle_C \geqslant 0.2$. The volume occupied by the vortices can be computed with a function I_Q which is equal to 1 for $Q/\langle S_{ij}S_{ij}\rangle_C \geqslant 0.2$ and 0 for $Q/\langle S_{ij}S_{ij}\rangle_C < 0.2$. The volume fraction of

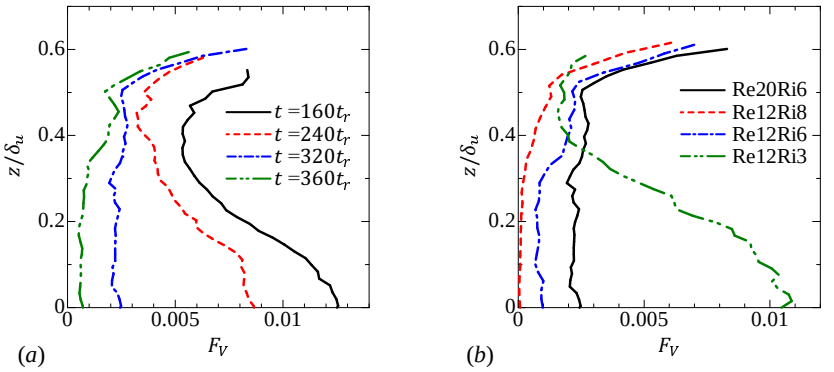

Figure 9: Volume fraction of vortices in turbulent regions, F_V, plotted as a function of z/δ_u, where vortices and turbulent regions are detected respectively by the conditions $Q/\langle S_{ij}S_{ij}\rangle_C \geqslant 0.2$ and $|\boldsymbol{\omega}| \geqslant 0.04\langle|\boldsymbol{\omega}|\rangle_C$. ($a$) Time dependence of F_V in Re20Ri6. (b) F_V at $t = 320t_r$ in all simulations.

the vortices in the turbulent region is computed with the intermittency factor $\gamma = \langle I\rangle$ as $F_V(z) = \langle I_Q\rangle/\gamma$, where the vertical profiles of γ is shown in figure 3(b). Here, F_V is computed in the region of $\gamma \geqslant 0.05$. Figure 9(a) shows the vertical profiles of F_V at different times in Re20Ri6. F_V is small because the distribution of the vortices is intermittent in space. Less than one percent of the middle of the shear layer is occupied by the vortices except at early time $t = 160t_r$. F_V in the middle of the shear layer is large at $t = 160t_r$, but decreases with time. At later times ($t = 320t_r$ and $360t_r$), F_V hardly depends on the vertical location in the middle of the shear layer. At these times, F_V increases with z for $z/\delta_u \geqslant 0.5$. Therefore, the vortices occupy larger volume of the turbulent region near the edge of the shear layer than the middle of the shear layer. Figure 9(b) shows F_V at $t = 320t_r$ in all simulations. As Re decreases or Ri increases, F_V near the centreline becomes smaller. Comparing figure 9(b) with table 1, one can see that F_V on the centreline tends to be smaller as Re_b decreases. Both F_V and Re_b decrease with time for the time period shown in figure 9(a). Thus, the volume fraction of the small-scale vortices decreases in the middle of the shear layer as Re_b decreases. Even after F_V becomes very small in the middle of the shear layer, F_V for $z/\delta_u \geqslant 0.5$ has larger values than in the middle. The small-scale vortices in the middle of the shear layer tend to disappear as Re_b decreases while the vortices can survive for longer time near the edge of the shear layer. Although F_V depends on the threshold used for defining the vortices, the results are qualitatively insensitive to the threshold, where the dependence of F_V on time, Re and Ri observed in figure 9 does not change with the threshold.

The orientation of vortices is examined by $\cos\theta_{\omega i} = \omega_i/|\boldsymbol{\omega}|$, where $\theta_{\omega i}$ is the angle between the i axis and the vorticity vector. Probability density functions (PDFs) of $\cos\theta_{\omega i}$ are computed from the regions with $Q/\langle S_{ij}S_{ij}\rangle_C \geqslant 0.3$, which are inside the isosurfaces used for visualizing the vortices in figures 6 and 7. Figure 10 shows the PDFs of $\cos\theta_{\omega x}$, $\cos\theta_{\omega y}$ and $\cos\theta_{\omega z}$ at (a, c, e) $t = 160t_r$ and (b, d, f) $t = 320t_r$. At $t = 160t_r$ and for $|z/\delta_u| \leqslant 0.4$, the PDF is large for $|\cos\theta_{\omega x}| \geqslant 0.75$, and the vortices in the middle of the shear layer tend to be oriented in the streamwise direction. The PDF is large for $\cos\theta_{\omega y} > 0$ while the PDF of $\cos\theta_{\omega z}$ is somewhat small only for $|\cos\theta_{\omega z}| > 0.7$. Thus, vortices can be oriented in various directions although there are a smaller number of vortices aligned in the vertical direction with $|\cos\theta_{\omega z}| \approx 1$. The preference for positive $\cos\theta_{\omega y}$ can be related to the mean shear $\partial\langle u\rangle/\partial z > 0$ that also contributes to positive

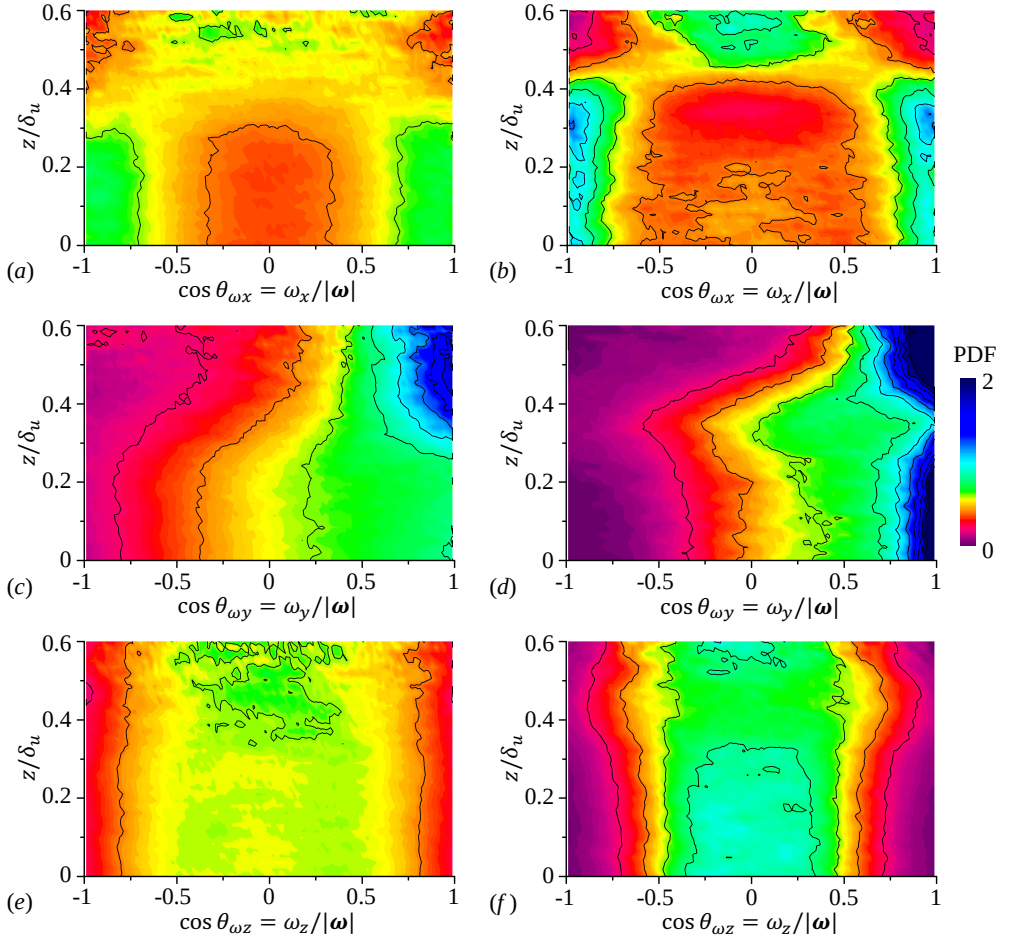

Figure 10: Probability density functions (PDFs) of $\cos\theta_{\omega i} = \omega_i/|\boldsymbol{\omega}|$ ($i = x, y$ or z) computed from the regions with $Q/\langle S_{ij}S_{ij}\rangle_C \geqslant 0.3$. $\theta_{\omega i}$ represents the angle between the i axis and vorticity vector. (a) $\cos\theta_{\omega x}$, (c) $\cos\theta_{\omega y}$ and (e) $\cos\theta_{\omega z}$ at $t = 160t_r$. (b) $\cos\theta_{\omega x}$, (d) $\cos\theta_{\omega y}$ and (f) $\cos\theta_{\omega z}$ at $t = 320t_r$.

spanwise vorticity. A large number of vortices inclined in the streamwise direction were also found in homogenous shear turbulence (Kida & Miura 1998). Therefore, the large probability for $|\cos\theta_{\omega x}| \geqslant 0.75$ is caused by the mean shear in the stably-stratified shear layer. Near the top of the shear layer at $t = 160t_r$, the PDFs are large for $\cos\theta_{\omega y} \approx 1$ and small for $|\cos\theta_{\omega x}| \approx \pm 1$. Thus, there are a large number of spanwise vortices in this region. The PDFs at $t = 320t_r$ in figure 10(b, d, f) have larger peaks than at $t = 160t_r$ in figure 10(a, c, e): the vortices at later time tend to align with specific directions, while they can be oriented in various directions at early time, as also confirmed in the visualizations (figure 8). The PDFs for $|z/\delta_u| \leqslant 0.4$ are very large for $\cos\theta_{\omega x} \approx \pm 1$ and $\cos\theta_{\omega y} \approx 1$, but are almost 0 for $\cos\theta_{\omega z} \geqslant 0.75$. Most of the vortices are streamwise or spanwise vortices that are almost perpendicular to the vertical direction. Visualizations in figure 7 also show a large number of horizontal vortices. The shape of the PDFs is different near the top of the shear layer, where the PDFs are large for $\cos\theta_{\omega y} \approx 1$ and small for $\cos\theta_{\omega x} \approx \pm 1$ and $\cos\theta_{\omega z} \approx \pm 1$. Therefore, most small-scale vortices are spanwise vortices at the top of

the shear layer. Figure 6 also shows that a large number of the heads of hairpin vortices are oriented in the spanwise direction.

The vortical structures in figure 6 clearly show that there are connections between the stably-stratified shear layer and wall-bounded shear flows. This implies that the structures related to the highly elongated pattern of u' in the x-y plane in figure 4 is the stably-stratified shear layer equivalent to the superstructure or very large-scale motion in wall-bounded shear flows. Flow visualizations related to these structures have been conducted in boundary layers, channel flows and pipe flows (Hutchins & Marusic 2007; Monty *et al.* 2007; Hellström *et al.* 2011; Lee & Sung 2013), where one can find highly elongated flow structures similar to figures 4(b, c). In turbulent boundary layers, the streamwise extent of the superstructures was found to be of the order of 10 times of the boundary layer thickness (Hutchins & Marusic 2007). The region of positive and negative u' in figure 4(c) also has a streamwise length of $\mathcal{O}(10\delta_u)$. We use the term "superstructure" to denote the structure related to the highly elongated region with positive or negative u'. It should be noted that the hairpin-shaped vortices cannot be found at earlier times, at which the small-scale vortices can be oriented in various directions as confirmed from figure 8(a). Our previous DNS of stably-stratified shear layers ($Re = 900$ and $Ri = 0.04$) also showed that small-scale vortices visualized with Q are randomly oriented at early time $t = 150t_r$, at which the buoyancy Reynolds number is 80 (Watanabe *et al.* 2016). The superstructures also become detectable in figure 4 only for $t \geqslant 240t_r$. The structures of stably-stratified shear layers at late times become similar to those in wall-bounded shear flows.

In Smyth & Moum (2000a), a few hairpin vortices can be found in the visualization of enstrophy in the DNS of the stably-stratified shear layer with a smaller computational domain than in the present DNS. The present study further confirms that the hairpin vortices are prominent near the top of the shear layer, and they can appear even in the middle of the shear layer. Hairpin vortices were also found in other stably-stratified turbulent shear flows. It was shown that hairpin vortices appear in turbulent Holmboe waves of stably-stratified shear layers (Smyth & Winters 2003; Smyth 2006). The Holmboe waves are dominant over the Kelvin-Helmholtz instability for high Richardson numbers, and are not addressed in this study. Pham *et al.* (2012) performed DNS of two parallel stably-stratified shear layers, where one of the shear layers develops into turbulence through the Kelvin-Helmholtz instability and interacts with another strongly stratified shear layer. Hairpin vortices were also found in their DNS when the turbulent shear layer begins to interact with the strongly-stratified shear layer. Field measurements of stratocumulus clouds (Katzwinkel *et al.* 2012; Malinowski *et al.* 2013) found a stably-stratified region with a wind shear at the stratocumulus top. In two-dimensional profiles of enstrophy taken from DNS of the stratocumulus top (Mellado *et al.* 2014; Mellado 2017), the stably-stratified sheared region exhibits enstrophy patterns of hairpin vortices similar to those in figure 8(b). These previous studies indicate that hairpin vortices can exist in various stably-stratified shear flows.

3.3. *Spectral analysis*

The energy spectrum of the streamwise velocity, E_{uu}, is computed using Fourier transforms in the streamwise direction. Figures 11(a-c) show the energy spectrum as functions of the streamwise wavelength $\lambda_x = 2\pi/k_x$ and the vertical location, where k_x is the streamwise wavenumber. The spectrum is multiplied by k_x to put the plots in area-preserving form. It is seen that $k_x E_{uu}$ substantially changes with time. In figure 11(a), at $t = 160t_r$, $k_x E_{uu}$ takes on a very large value at $\lambda_x/\delta_u \approx 2.0$-$2.5$. At the later times shown in figures 11(b) and (c), $k_x E_{uu}$ exhibits two peaks at distinct wavelengths for

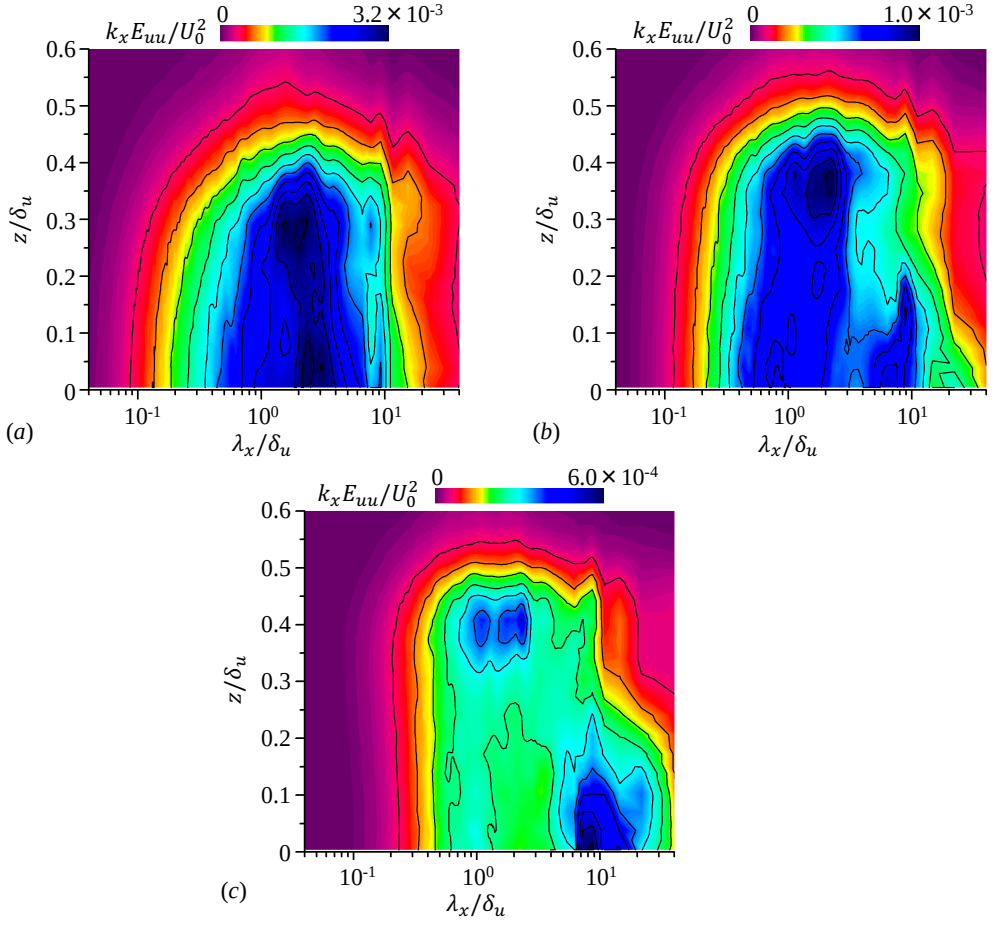

Figure 11: Spectra of streamwise velocity fluctuation k_xE_{uu}. (*a*) $t = 160t_r$, (*b*) $t = 240t_r$ and (*c*) $t = 320t_r$ of Re20Ri6. Spectra are shown as a function of the vertical location z and the streamwise wavelength $\lambda_x = 2\pi/k_x$.

$z/\delta_u \lesssim 0.2$. At $z = 0$ in figure 11(*c*), the shorter wavelength peak occurs at $\Lambda_S = 1.0\delta_u$ while the longer wavelength peak is found at $\Lambda_L = 8.7\delta_u$. The wavelengths Λ_S and Λ_L at $z = 0$ are shown with arrows in figures 4(*b*) and (*c*). From these two figures one can see that the streamwise extent of the superstructures is close to the wavelength Λ_L. The shorter wavelength peak, at $\Lambda_S \sim \delta_u$, is close to the shear layer thickness, which is of the same order as the streamwise length of the region of $u' < 0$ near the hairpin vortex in figure 6. Similarly, the spectrum of streamwise velocity with two peaks was also reported in wall turbulence (Guala *et al.* 2006; Lee & Moser 2015). In figure 11(*c*), Λ_L only weakly depends on the vertical location for $z/\delta_u \lesssim 0.2$. This differs from the spectrum of streamwise velocity in channel and pipe flows, where the peak wavelength Λ_L associated with very large-scale motions becomes larger with the distance from the wall (Monty *et al.* 2009). In the region of $0.2 \leqslant z/\delta_u \leqslant 0.4$, the spectral shape in figure 11(*c*) changes with vertical location from a bimodal profile to a unimodal profile. The peak at Λ_L does not exist near the top of the shear layer ($z/\delta_u \gtrsim 0.3$), where k_xE_{uu} is large for $\lambda_x \sim \delta_u$. Similarly, the spectrum in turbulent boundary layers has a peak

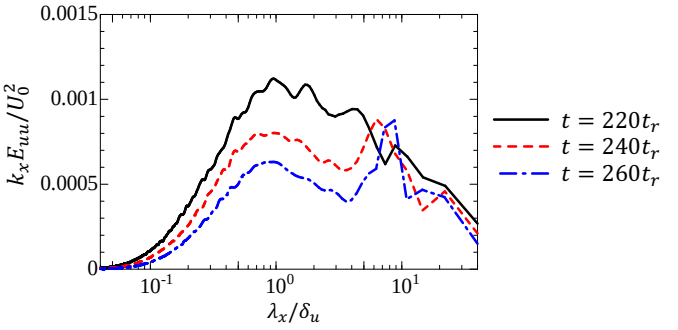

Figure 12: Spectra of streamwise velocity fluctuation k_xE_{uu} on the centreline of Re20Ri6.

associated with the superstructure near the wall, but this peak disappears in the outer region (Monty *et al.* 2009). Although the shorter peak-wavelength Λ_S weakly depends on the vertical location, the peak value of k_xE_{uu} around Λ_S is higher near the top of the shear layer than in the middle.

Figure 12 shows k_xE_{uu} on the centreline at $t = 220t_r$, $240t_r$ and $260t_r$. The change in the spectral shape occurs between $t = 220t_r$ and $240t_r$, and the double peaks discussed above can be seen from $t = 240t_r$. The shorter peak-wavelength Λ_S divided by δ_u at $t = 240t_r$ is close to that at later times while the longer peak-wavelength Λ_L/δ_u slightly increases with time.

Energy spectra of the spanwise velocity, the vertical velocity and the density at $t = 320t_r$ are shown in figures 13(a), (b) and (c), respectively. Double peaks in these spectra can be seen in the middle of the shear layer. Near the top of the shear layer ($z/\delta_u \approx 0.4$), a relatively large amount of energy of the vertical velocity is at the scales of $\lambda_x/\delta_u \approx 0.5$, and the vertical motion is still active even at large scales. This is even though this scale is much larger than Ozmidov scale, which is often interpreted as the largest horizontal scale that can overturn (Riley & Lindborg 2008). The peaks in k_xE_{vv} and k_xE_{ww} appear at $\lambda_x/\delta_u \approx 0.5$ on the centreline. This length is about half of the shorter peak-wavelength $\lambda_x/\delta_u \approx 1.0$ in k_xE_{uu}. The peak wavelengths of k_xE_{vv} and k_xE_{ww} are related to the transverse integral length scale while that of k_xE_{uu} is related to the longitudinal integral length scale. In homogeneous isotropic turbulence, the transverse integral length scale L_T is half of the longitudinal one L (Pope 2000). L_T/L is about 0.4 even in a turbulent circular jet (Antonia & Zhao 2001). This ratio can explain the observed difference in the peak wavelength in k_xE_{uu}, k_xE_{vv} and k_xE_{ww}.

Figures 14(a) and (b) show the cospectra at $t = 320t_r$ between u' and w' (C_{uw}) and between ρ' and w' ($C_{\rho w}$), whose corresponding integrals give the vertical turbulent fluxes of streamwise momentum $\langle u'w' \rangle$ and density $\langle \rho'w' \rangle$. It should be noted that negative $u'w'$ and positive $\rho'w'$ are associated with a flux of heavier fluid with negative streamwise velocity from the lower side of the shear layer to the upper side, and vice-versa. In non-stratified turbulent shear layers, turbulent motions generally contribute to negative $u'w'$ and positive $\rho'w'$ (Rogers & Moser 1994). For $\lambda_x/\delta_u \approx 0.5$, all vertical locations have $C_{uw} < 0$ and $C_{\rho w} > 0$, and turbulent mixing is very active at this length scale. This wavelength is also close to the streamwise length of the hairpin vortices, which is associated with the region of $u'w' < 0$ in figure 6(c). The velocity vectors in figure 6(c) indicate that the heads of the hairpin vortices can contribute to $u'w' < 0$. Both signs of C_{uw} and $C_{\rho w}$ appear at the wavelength around $\Lambda_L \approx 9\delta_u$. Note that a stably-stratified fluid can support the propagation of the internal gravity wave-like motions, for which

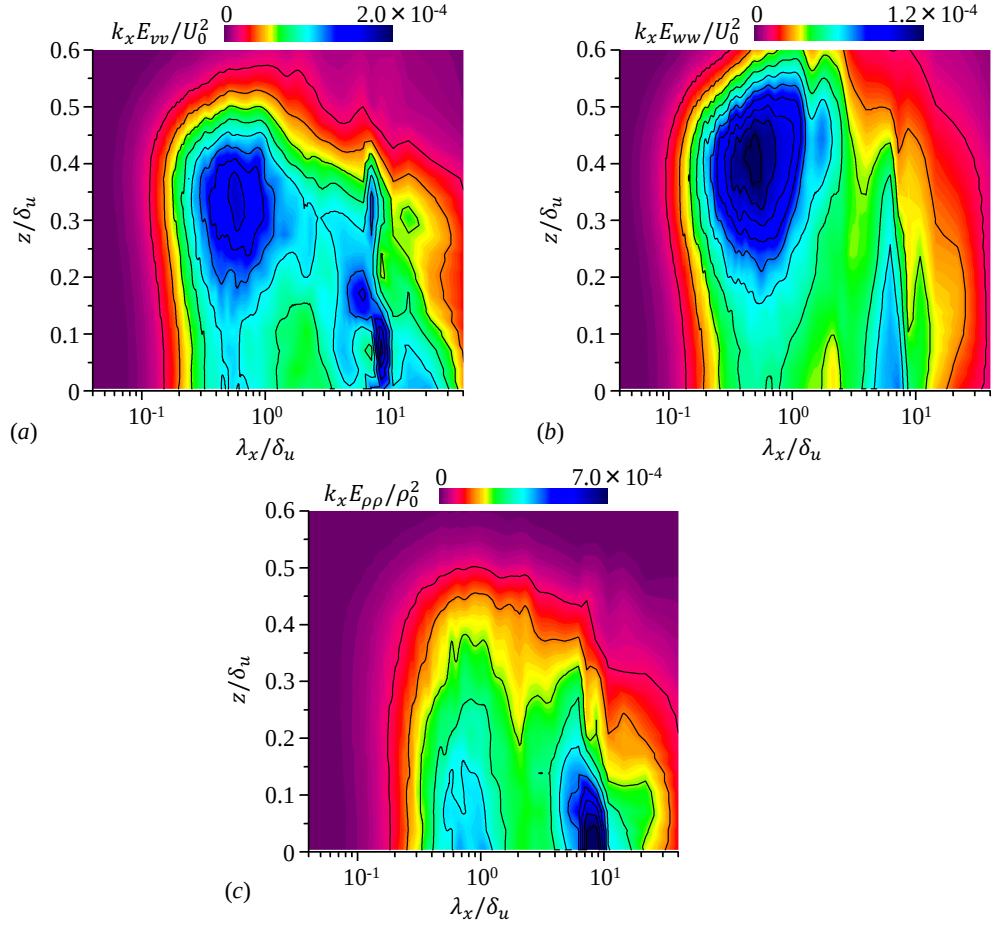

Figure 13: Spectra of (a) spanwise velocity fluctuation k_xE_{vv}, (b) vertical velocity fluctuation k_xE_{ww} and (c) density fluctuation $k_xE_{\rho\rho}$ at $t = 320t_r$ of Re20Ri6.

$\rho'w'$ can take on both positive or negative values depending on the phase of the wave. Oscillation in buoyancy flux $\langle\rho'w'\rangle$ has been also observed as the wave-like features in stably stratified turbulence (Venayagamoorthy & Stretch 2006). Although it is difficult to observe the wave motions directly in the visualizations, very large scales affected by the superstructures might behave like a wave that has both negative and positive values of $\rho'w'$ and $u'w'$. The convergence of the cospectra at large scales is not as good as at small scales. The change in sign of the cospectra at large scales can be caused by an insufficient convergence of averages computed with large positive and negative fluctuations of $\rho'w'$ and $u'w'$ in wavenumber space.

Figures 15(a) and (b) compare, for all the simulations, the shape of the spectra k_xE_{uu} normalized by u_{rms}^2 at $z = 0$ and $z = 0.4\delta_u$ for $t = 320t_r$. Values of δ_u, L_O, η, Re_b and Ri_g at $z = 0$ and $t = 320t_r$ are summarized in table 1. In figure 15(a), the large peak for $\lambda_x/\delta_u > 1$ appears in all the simulations, but the peak wavelength differs for Re12Ri3, which has the lowest Richardson number. In contrast, the spectra at $z = 0.4\delta_u$ have a qualitatively similar shape for all simulations as seen in figure 15(b), where the peak wavelength Λ_S can be related to the streamwise length of the hairpin vortex structures.

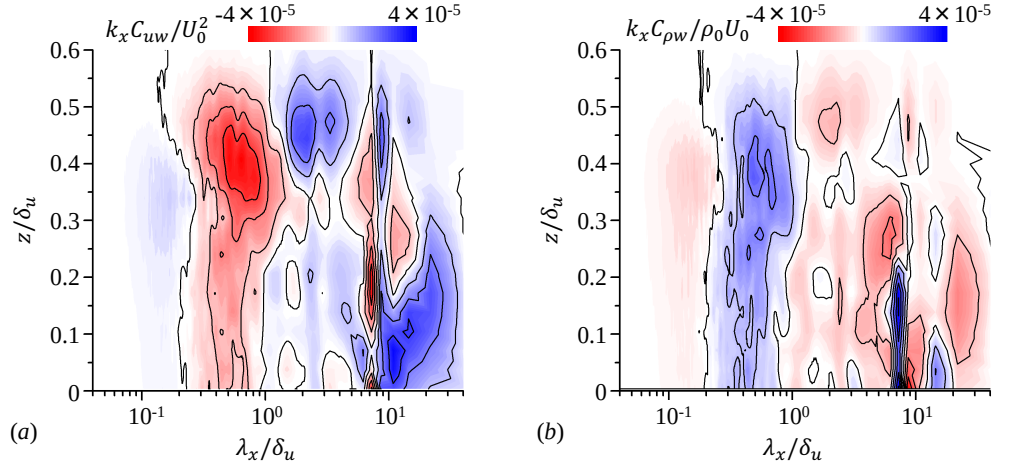

Figure 14: Cospectra of (a) streamwise and vertical velocity fluctuations $k_x C_{uw}$, and (b) of the density and vertical velocity fluctuations $k_x C_{\rho w}$ at $t = 320t_r$ of Re20Ri6.

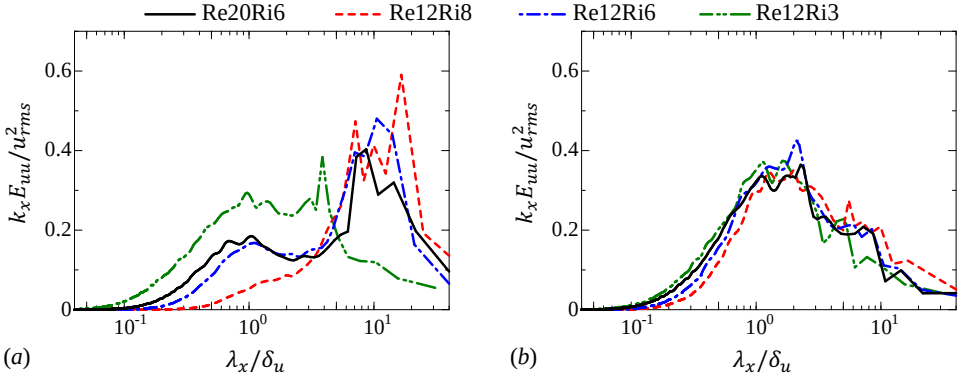

Figure 15: Comparison of energy spectra of streamwise velocity fluctuations $k_x E_{uu}$ among all DNSs at $t = 320t_r$ at (a) $z = 0$ and (b) $z = 0.4\delta_u$.

At both vertical locations, one can also see that the fraction of the energy in small scales $\lambda_x < \delta_u$ decreases as Ri increases or Re decreases. The energy distribution in the spectral space at $z = 0$ depends strongly on Re and Ri. In particular, the scales smaller than δ_u in Re12Ri8 have only a small amount of energy at $z = 0$. However, the energy fraction at small scales at $z = 0.4\delta_u$ for Re12Ri8 is comparable to those in other cases, and the small-scale motions can survive longer near the edge than the middle of the shear layer. Two peaks of $k_x E_{uu}$ on the centreline are expected to be clearly observed when Λ_S and Λ_L are well separated. The shorter peak-wavelength Λ_S is close to the shear layer thickness δ_u while the longer peak-wavelength Λ_L divided by δ_u increases with time in figure 12. In figure 15(a), the longer peak-wavelength Λ_L/δ_u is smaller in Re12Ri3 than in other cases. Therefore, Λ_L/Λ_S becomes larger with time or as Ri increases. Figures 12 and 15(a) indicate that as the turbulence decays with time, the shorter-wavelength peak near the centreline decreases and eventually disappears. This happens at earlier time for lower Reynolds number or higher Richardson number, as confirmed in figure 15(a).

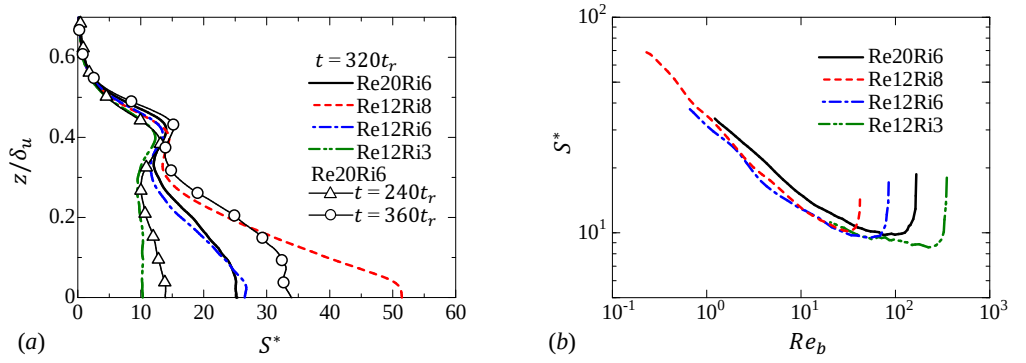

Figure 16: (a) Vertical profiles of integral shear parameter S^*. (b) S^* against Re_b on the centreline in the decay period of Re_b.

The two spectral peaks on the centreline can be found when the short-wavelength peak survives until the scale separation Λ_L/Λ_S becomes large.

3.4. *Integral shear parameter*

One of the important and common features when comparing the stably-stratified shear layer and wall-bounded shear flows is the production of turbulence by mean shear under circumstances in which vertical motions are suppressed by the buoyancy or by the wall. The timescale of the mean shear is defined by $\tau_S = S^{-1} = (\partial\langle u\rangle/\partial z)^{-1}$. The turbulent production is related to the coupling between the mean shear and eddies with the integral length scale $L_\varepsilon = q^3/\varepsilon$ and velocity scale $q = \langle u_i' u_i'\rangle^{1/2}$. This coupling can be studied with the timescale ratio of the eddy turnover time L_ε/q to τ_S given by $S^* = Sq^2/\varepsilon$, which is called the integral shear parameter (Jiménez 2018). When $S^* \ll 1$, the eddies evolve much faster than the shear timescale, and there is very little direct interaction between the eddies and the mean shear. On the other hand, when $S^* \gg 1$, the evolution of the eddies are strongly influenced by the shear.

Figure 16(a) shows the vertical profile of S^* in the stably-stratified shear layer for the various simulations. S^* in the middle of the shear layer strongly depends on time and Ri. One can see from case Re20Ri6 that, in the region near the centreline, $S^* \approx$ 12-14 until $t = 240t_r$, and then S^* begins to rapidly increase up to about 35 at $t/t_r = 360$. Values of S^* near $z = 0$ also increase as Ri increases at $t/t_r = 320$. Figure 16(b) shows variations of S^* against Re_b at $z = 0$ in the decay period of Re_b. The relation between S^* and Re_b is similar in all simulations: $S^* \approx 10$ for $Re_b \gtrsim 10$, and S^* begins to increase with the decay of Re_b. In contrast, in the region near the top of the layer ($z/\delta_u \gtrsim 0.35$) $S^* \approx 13$ independently of time, Re and Ri. Once S^* increases near the centreline, the vertical variation in S^* becomes similar to those in wall-bounded shear flows, where S^* decreases from the buffer layer with $S^* \approx$ 30-40 to the logarithmic layer with $S^* \approx 10$ (Jiménez 2013). The hairpin vortices and superstructures are found in the stably-stratified shear layer after S^* on the centreline has begun to increase for $t \geqslant 240t_r$. A similar value $S^* \approx 10$ is also obtained in statistically stationary and homogeneous shear turbulence, whose connection to the logarithmic layer is pointed out in Sekimoto *et al.* (2016). Table 1 summarizes L_ε at $z = 0$ at $t/t_r = 320$. L_ε is slightly smaller than δ_u, and is coincident with the scales at which turbulent kinetic energy and density fluctuations are produced ($C_{uw} < 0$ and $C_{\rho w} > 0$ in figure 14). A moderately large value $S^* \approx 10$ near the top of

the shear layer implies that the interaction between the motion at the integral scale and the mean shear is quasilinear in this region (Jiménez 2018).

4. Conclusions

Direct numerical simulations in a very large computational domain have allowed the investigation of both large-scale and small-scale turbulent structures in stably-stratified shear layers. Turbulent structures which appear in stably-stratified shear layers at later times are very similar to some of the turbulent structures observed in wall-bounded shear flows. For example, hairpin vortices exist as small-scale vortical structures in the stably-stratified shear layers. In the middle of the shear layer, many small-scale vortices are oriented in streamwise or spanwise directions. These streamwise and spanwise vortices can be the legs and heads of the hairpin vortices. On the other hand, a large number of spanwise vortices appear as the heads of the hairpin vortices near the top of the shear layer. The pattern of streamwise velocity fluctuations clearly confirmed the existence of highly elongated structures with positive and negative streamwise velocity fluctuations (superstructures), whose streamwise length scale can be of the order of 10 times the thickness of the stably-stratified shear layer. The spectra of velocity and density exhibit large peaks at the wavenumbers associated with the streamwise length of these structures.

It was shown that the superstructures appear in the middle of the shear layer while the hairpin vortices exist in the entire layer. The small-scale vortical structures including hairpin vortices appear intermittently. In the upper side of the shear layer, where the mean streamwise velocity is positive, more small-scale vortical structures appear over the region with negative streamwise velocity fluctuations. The flow patterns associated with hairpin vortices can cause turbulent mixing by transferring heavy fluid from the lower region in the upward direction, and vice-versa for lighter fluid. Cospectra related to vertical turbulent fluxes of momentum and density clearly show that turbulent mixing is very active at the length scales close the streamwise extent of the hairpin vortices, although this scale is much larger than the Ozmidov scale.

These structural similarities with wall-bounded shear flows become clearer at later times, when the integral shear parameter S^* begins to increase toward values of about 30 to 50 near the centreline and about 10 near the top of the shear layer. These values of S^* are close to the values of about 30 in the buffer layer and about 10 in the logarithmic layer in wall-bounded shear flows. The value of S^* of about 10 near the edge of the stably-stratified shear layer only weakly depends on time and initial Reynolds and Richardson numbers. A large amount of the kinetic energy occurs at scales close to the shear layer thickness, which is also the length scale of the velocity fluctuations associated with the hairpin vortices.

The direct numerical simulations presented in this manuscript were carried out on the high-performance computing system (NEC SX-ACE) in the Japan Agency for Marine-Earth Science and Technology. This work was partially supported by "Collaborative Research Project on Computer Science with High-Performance Computing in Nagoya University" and by JSPS KAKENHI Grant Number 18K13682 and 18H01367.

REFERENCES

Adrian, R. J., Meinhart, C. D. & Tomkins, C. D. 2000 Vortex organization in the outer region of the turbulent boundary layer. *J. Fluid Mech.* **422**, 1–54.

Antonia, R. A. & Zhao, Q. 2001 Effect of initial conditions on a circular jet. *Exp. Fluids* **31** (3), 319–323.

Barry, M. E., Ivey, G. N., Winters, K. B. & Imberger, J. 2001 Measurements of diapycnal diffusivities in stratified fluids. *J. Fluid Mech.* **442**, 267–291.

Brucker, K. A. & Sarkar, S. 2007 Evolution of an initially turbulent stratified shear layer. *Phys. Fluids* **19** (10), 105105.

Carlier, J. & Stanislas, M. 2005 Experimental study of eddy structures in a turbulent boundary layer using particle image velocimetry. *J. Fluid Mech.* **535**, 143–188.

Corrsin, S. & Kistler, A. L. 1955 Free-stream boundaries of turbulent flows. *NACA Technical Report No. TN-1244* .

Davidson, P. A. 2004 *Turbulence: An Introduction for Scientists and Engineers*. Oxford Univ. Pr.

De Silva, I. P. D., Fernando, H. J. S., Eaton, F. & Hebert, D. 1996 Evolution of Kelvin-Helmholtz billows in nature and laboratory. *Earth Planet. Sci. Lett.* **143** (1), 217–231.

Dennis, D. J. C. & Nickels, T. B. 2011 Experimental measurement of large-scale three-dimensional structures in a turbulent boundary layer. Part 1. vortex packets. *J. Fluid Mech.* **673**, 180–217.

Fernando, H. J. S. 1991 Turbulent mixing in stratified fluids. *Annu. Rev. Fluid Mech.* **23** (1), 455–493.

Guala, M., Hommema, S. E. & Adrian, R. J. 2006 Large-scale and very-large-scale motions in turbulent pipe flow. *J. Fluid Mech.* **554**, 521–542.

Head, M. R. & Bandyopadhyay, P. 1981 New aspects of turbulent boundary-layer structure. *J. Fluid Mech.* **107**, 297–338.

Hellström, L. H. O., Sinha, A. & Smits, A. J. 2011 Visualizing the very-large-scale motions in turbulent pipe flow. *Phys. Fluids* **23** (1), 011703.

Hutchins, N. & Marusic, I. 2007 Evidence of very long meandering features in the logarithmic region of turbulent boundary layers. *J. Fluid Mech.* **579**, 1–28.

Jiménez, J. 2013 How linear is wall-bounded turbulence? *Phys. Fluids* **25** (11), 110814.

Jiménez, J. 2018 Coherent structures in wall-bounded turbulence. *J. Fluid Mech.* **842**.

Katzwinkel, J., Siebert, H. & Shaw, R. A. 2012 Observation of a self-limiting, shear-induced turbulent inversion layer above marine stratocumulus. *Boundary-Layer Meteorol.* **145** (1), 131–143.

Kempf, A., Klein, M. & Janicka, J. 2005 Efficient generation of initial-and inflow-conditions for transient turbulent flows in arbitrary geometries. *Flow, Turbul. Combust.* **74** (1), 67–84.

Kida, S. & Miura, H. 1998 Identification and analysis of vortical structures. *Eur. J. Mech. B* **17** (4), 471–488.

Kim, K. C. & Adrian, R. J. 1999 Very large-scale motion in the outer layer. *Phys. Fluids* **11** (2), 417–422.

Krug, D., Holzner, M., Lüthi, B., Wolf, M., Kinzelbach, W. & Tsinober, A. 2015 The turbulent/non-turbulent interface in an inclined dense gravity current. *J. Fluid Mech.* **765**, 303–324.

de Lavergne, C., Madec, G., Le Sommer, J., Nurser, A. J. G. & Naveira Garabato, A. C. 2016 The impact of a variable mixing efficiency on the abyssal overturning. *J. Phys. Oceanogr.* **46** (2), 663–681.

Lee, J. H. & Sung, H. J. 2013 Comparison of very-large-scale motions of turbulent pipe and boundary layer simulations. *Phys. Fluids* **25** (4), 045103.

Lee, M. & Moser, R. D. 2015 Direct numerical simulation of turbulent channel flow up to $Re_\tau \approx 5200$. *J. Fluid Mech.* **774**, 395–415.

Malinowski, S. P., Gerber, H., Plante, J.-L., Kopec, M. K., Kumala, W., Nurowska, K., Chuang, P. Y., Khelif, D., Haman, K. E. & others 2013 Physics of Stratocumulus Top (POST): turbulent mixing across capping inversion. *Atmos. Chem. Phys* **13** (24), 12171–12186.

Mashayek, A., Caulfield, C. P. & Peltier, W. R. 2017 Role of overturns in optimal mixing in stratified mixing layers. *J. Fluid Mech.* **826**, 522–552.

Mashayek, A. & Peltier, W. R. 2012*a* The 'zoo' of secondary instabilities precursory to stratified shear flow transition. Part 1 Shear aligned convection, pairing, and braid instabilities. *J. Fluid Mech.* **708**, 5–44.

Mashayek, A. & Peltier, W. R. 2012*b* The 'zoo'of secondary instabilities precursory to

stratified shear flow transition. Part 2 The influence of stratification. *J. Fluid Mech.* **708**, 45–70.

Mathis, R., Hutchins, N. & Marusic, I. 2009 Large-scale amplitude modulation of the small-scale structures in turbulent boundary layers. *J. Fluid Mech.* **628**, 311–337.

Mellado, J. P. 2017 Cloud-top entrainment in stratocumulus clouds. *Annu. Rev. Fluid Mech.* **49**, 145–169.

Mellado, J. P., Stevens, B. & Schmidt, H. 2014 Wind shear and buoyancy reversal at the top of stratocumulus. *J. Atmos. Sci.* **71** (3), 1040–1057.

Monty, J. P., Hutchins, N., Ng, H. C. H., Marusic, I. & Chong, M. S. 2009 A comparison of turbulent pipe, channel and boundary layer flows. *J. Fluid Mech.* **632**, 431–442.

Monty, J. P., Stewart, J. A., Williams, R. C. & Chong, M. S. 2007 Large-scale features in turbulent pipe and channel flows. *J. Fluid Mech.* **589**, 147–156.

Moum, J. N. 1996 Efficiency of mixing in the main thermocline. *J. Geophys. Res.* **101** (C5), 12057–12069.

Ooi, A., Martin, J., Soria, J. & Chong, M. S. 1999 A study of the evolution and characteristics of the invariants of the velocity-gradient tensor in isotropic turbulence. *J. Fluid Mech.* **381**, 141–174.

Peltier, W. R. & Caulfield, C. P. 2003 Mixing efficiency in stratified shear flows. *Annu. Rev. Fluid Mech.* **35** (1), 135–167.

Pham, H. T., Sarkar, S. & Winters, K. B. 2012 Intermittent patches of turbulence in a stratified medium with stable shear. *J. Turbulence* (13), N20.

Pope, S. B. 2000 *Turbulent Flows*. Cambridge Univ. Pr.

Riley, J. J. & Lindborg, E. 2008 Stratified turbulence: A possible interpretation of some geophysical turbulence measurements. *J. Atmos. Sci.* **65** (7), 2416–2424.

Robinson, S. K. 1991 Coherent motions in the turbulent boundary layer. *Annu. Rev. Fluid Mech.* **23** (1), 601–639.

Rogers, M. M. & Moser, R. D. 1994 Direct simulation of a self-similar turbulent mixing layer. *Phys. Fluids* **6** (2), 903–923.

Salehipour, H, Peltier, WR & Mashayek, A 2015 Turbulent diapycnal mixing in stratified shear flows: the influence of Prandtl number on mixing efficiency and transition at high Reynolds number. *J. Fluid Mech.* **773**, 178–223.

Schoppa, W. & Hussain, F. 2002 Coherent structure generation in near-wall turbulence. *J. Fluid Mech.* **453**, 57–108.

Sekimoto, A., Dong, S. & Jiménez, J. 2016 Direct numerical simulation of statistically stationary and homogeneous shear turbulence and its relation to other shear flows. *Phys. Fluids* **28** (3), 035101.

Shih, L. H., Koseff, J. R., Ivey, G. N. & Ferziger, J. H. 2005 Parameterization of turbulent fluxes and scales using homogeneous sheared stably stratified turbulence simulations. *J. Fluid Mech.* **525**, 193–214.

da Silva, C. B., Dos Reis, R. J. N. & Pereira, J. C. F. 2011 The intense vorticity structures near the turbulent/non-turbulent interface in a jet. *J. Fluid Mech.* **685**, 165–190.

da Silva, C. B., Hunt, J. C. R., Eames, I. & Westerweel, J. 2014 Interfacial layers between regions of different turbulence intensity. *Annu. Rev. Fluid Mech.* **46**, 567–590.

da Silva, C. B. & Pereira, J. C. F. 2008 Invariants of the velocity-gradient, rate-of-strain, and rate-of-rotation tensors across the turbulent/nonturbulent interface in jets. *Phys. Fluids* **20** (5), 055101.

Smyth, W. D. 2006 Secondary circulations in Holmboe waves. *Phys. Fluids* **18** (6), 064104.

Smyth, W. D. & Moum, J. N. 2000*a* Anisotropy of turbulence in stably stratified mixing layers. *Phys. Fluids* **12** (6), 1343–1362.

Smyth, W. D. & Moum, J. N. 2000*b* Length scales of turbulence in stably stratified mixing layers. *Phys. Fluids* **12** (6), 1327–1342.

Smyth, W. D. & Winters, K. B. 2003 Turbulence and mixing in Holmboe waves. *J. Phys. Oceanogr.* **33** (4), 694–711.

Strang, E. J. & Fernando, H. J. S. 2001 Entrainment and mixing in stratified shear flows. *J. Fluid Mech.* **428**, 349–386.

Thorpe, SA 1973*a* Experiments on instability and turbulence in a stratified shear flow. *Journal of Fluid Mechanics* **61** (4), 731–751.

Thorpe, SA 1973*b* Turbulence in stably stratified fluids: A review of laboratory experiments. *Bound.-Layer Meteor.* **5** (1-2), 95–119.

Venayagamoorthy, S. K. & Stretch, D. D. 2006 Lagrangian mixing in decaying stably stratified turbulence. *J. Fluid Mech.* **564**, 197–226.

Watanabe, T., Riley, J. J. & Nagata, K. 2016 Effects of stable stratification on turbulent/nonturbulent interfaces in turbulent mixing layers. *Phys. Rev. Fluids* **1** (4), 044301.

Watanabe, T., Riley, J. J. & Nagata, K. 2017 Turbulent entrainment across turbulent-nonturbulent interfaces in stably stratified mixing layers. *Phys. Rev. Fluids* **2** (10), 104803.

Watanabe, T., Riley, J. J., Nagata, K., Onishi, R. & Matsuda, K. 2018 A localized turbulent mixing layer in a uniformly stratified environment. *J. Fluid Mech.* **849**, 245–276.

Williams, O. J. H. 2014 Density effects on turbulent boundary layer structure: from the atmosphere to hypersonic flow. *PhD thesis, Princeton University* .

Woods, J. D. 1968 Wave-induced shear instability in the summer thermocline. *J. Fluid Mech.* **32** (4), 791–800.

Wu, X., Baltzer, J. R. & Adrian, R. J. 2012 Direct numerical simulation of a $30r$ long turbulent pipe flow at $r^+ = 685$: large-and very large-scale motions. *J. Fluid Mech.* pp. 235–281.

Wu, X. & Moin, P. 2009 Direct numerical simulation of turbulence in a nominally zero-pressure-gradient flat-plate boundary layer. *J. Fluid Mech.* **630**, 5–41.

Zhou, J., Adrian, R. J., Balachandar, S. & Kendall, T. M. 1999 Mechanisms for generating coherent packets of hairpin vortices in channel flow. *J. Fluid Mech.* **387**, 353–396.